

Enhanced screening and spectral diversity in many-body elastic scattering of excitons in two-dimensional hybrid metal-halide perovskites

Félix Thouin,¹ Daniele Cortecchia,² Annamaria Petrozzi,²
Ajay Ram Srimath Kandada,² and Carlos Silva^{3,1}

¹*School of Physics, Georgia Institute of Technology,
837 State Street NW, Atlanta, Georgia 30332, United States*

²*Center for Nano Science and Technology@PoliMi,
Istituto Italiano di Tecnologia, via Giovanni Pascoli 70/3, 20133 Milano, Italy*

³*School of Chemistry and Biochemistry,
Georgia Institute of Technology, 901 Atlantic Drive NW,
Atlanta, Georgia 30332, United States*

(Dated: December 15, 2024)

In two-dimensional hybrid organic-inorganic metal-halide perovskites, the intrinsic optical excitation lineshape reflects multiple excitons with distinct binding energies,¹ which are dressed differently by the hybrid lattice.² Given this complexity, a fundamentally far-reaching issue is how Coulomb-mediated many-body interactions — elastic scattering such as excitation-induced dephasing,³ inelastic exciton bimolecular scattering,⁴ and multi-exciton binding^{5,6} — depend upon the specific exciton-lattice coupling within the structured excitation lineshape. We measure the intrinsic and density-dependent exciton dephasing rates of the multiple excitons and their dependence on temperature by means of two-dimensional coherent excitation spectroscopy. We find that diverse excitons display distinct intrinsic dephasing rates mediated by phonon scattering involving different effective phonons, and contrasting rates of exciton-exciton elastic scattering. These findings establish specifically the consequence of distinct lattice dressing on exciton many-body quantum dynamics, which critically define fundamental optical properties that underpin photonics and quantum optoelectronics.

Spectral linewidths of optical transitions provide pertinent insights into the system-bath interactions in materials because they depend on optical dephasing dynamics — the processes by which the induced coherence in the optical response dissipates due to scattering processes with lattice phonons, other excitations, and defects. Dephasing rates thus are very sensitive probes of the consequences of lattice dressing effects on exciton properties. Nevertheless, in condensed matter, these are challenging to extract directly from linear optical probes such as absorption or photoluminescence spectroscopy given that the experimental linewidths typically arise from two distinct contributions: homogenous and inhomogenous broadening (see Fig. 1a). While the former is due to dephasing and is governed by the intrinsic finite lifetime of excited states and by dynamic disorder, the latter is caused by a statistical distribution of the transition energy due to static disorder, defects or grain boundaries. The exciton homogeneous linewidth 2γ (full width at half maximum) is limited by the exciton lifetime (Γ^{-1}) and the dephasing rate mediated by excitation-induced dephasing ($\gamma_{\text{EID}}/\hbar$) and phonon scattering (γ_{ph}/\hbar):

$$\gamma = \frac{\hbar\Gamma}{2} + \gamma_{\text{EID}} + \gamma_{\text{ph}}. \quad (1)$$

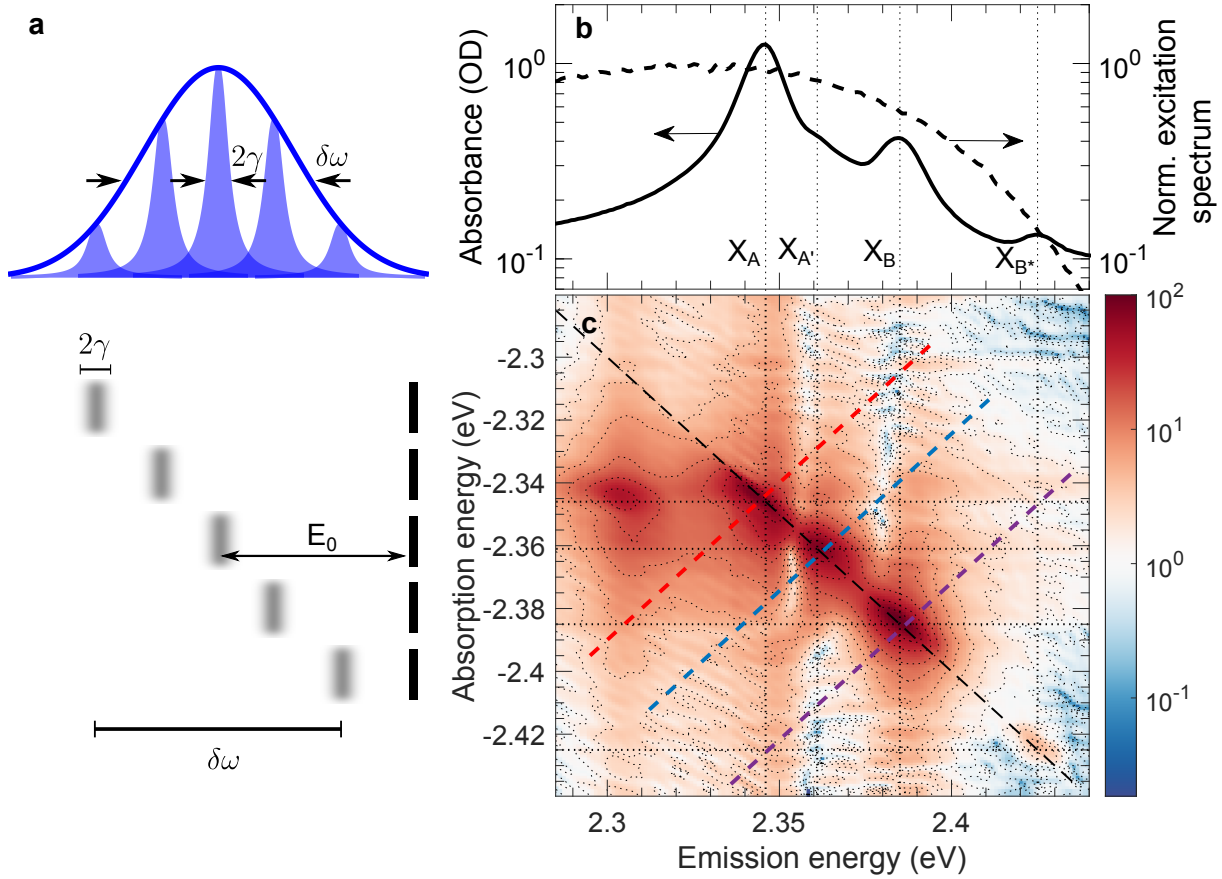


FIG. 1. Linear and two-dimensional coherent spectroscopy of $(\text{PEA})_2\text{PbI}_4$ at 5 K. (a) Illustration of the inhomogeneous and homogeneous nature of line broadening. The total linewidth (blue line) is composed of a distribution of homogeneously broadened lines (blue areas). This arises from the simultaneous existence of uncorrelated transitions from the ground state (black lines) to short-lived excited states (blurred lines). (b) Absorption spectrum of $(\text{PEA})_2\text{PbI}_4$ measured at 5 K (black line) and normalized spectrum of the pulses used in 2D coherent excitation spectroscopy measurements (dashed line). Both scales are logarithmic. Dotted lines indicate the energy of excitons A, A', B, and B*, respectively, with increasing energy. E_0 represents the central energy, $\delta\omega$ and 2γ the inhomogeneous and homogeneous linewidths respectively. (c) Absolute value of the 2D coherent rephasing spectrum of $(\text{PEA})_2\text{PbI}_4$ measured at 5 K with a pulse fluence of 40 nJ/cm^2 and a pump-probe delay of 20 fs. The color scale is logarithmic. Dotted lines indicate the energies of the aforementioned features. The paths of the diagonal cut (black dashed line) and anti-diagonal cuts at the diagonal energy of excitons A, A' and B (red, blue and purple dashed lines, respectively) are also shown.

An accurate estimate of γ is thus crucial to quantify the magnitude of the inter-exciton and exciton-phonon scattering cross-sections which subsequently determine the radiative rates and transport characteristics. It is possible to analyze temperature-dependent linear optical spectra to estimate the homogeneous linewidths, but this is an indirect approach as one can only measure the total linewidth. Shown in Fig. 1b is the linear absorption spectrum of a polycrystalline thin film of single-layered $(\text{PEA})_2\text{PbI}_4$ (PEA = phenylethylammonium) measured at 5 K. Four distinct excitonic features (later referred to as excitons A, A', B and B*), are observed about 200 meV below the continuum band edge (see Supporting information Fig. S1 for the temperature-dependent absorption spectra). Here, we implement a nonlinear coherent spectroscopy in order to unambiguously extract the homogeneous dephasing rates of the various excitonic transitions.

Four-wave-mixing spectroscopic techniques permit measurement of a third-order polarization induced in matter by a sequence of at least two femtosecond pulses (three in the present work) with well defined phase relationship, and the dissipation of this coherent contribution to the total polarization reports directly on dephasing processes. In a two-dimensional coherent excitation geometry with so-called rephasing phase matching, one measures a two-dimensional spectral correlation map with two independent energy variables, the absorption energy E_{abs} and the emission energy E_{em} . Along the $E_{\text{abs}} = E_{\text{em}}$ diagonal axis, one observes the individual exciton resonances identified in the linear absorption spectrum, with any off-diagonal cross peaks displaying spectral correlations between the various excitonic transitions. Importantly, this 2D lineshape permits separation of the homogeneous and inhomogeneous contributions to the optical linewidth. Specifically, if the homogeneous and inhomogeneous linewidths are comparable, which is the case in $(\text{PEA})_2\text{PbI}_4$,⁶ global analysis of the diagonal and antidiagonal lineshapes enables an accurate estimation of the dephasing parameter γ :^{7,8}

$$S_{AD}(\omega_{ad}) = \left| \frac{\exp\left(\frac{(\gamma-i\omega_{ad})^2}{2\delta\omega^2}\right) \text{erfc}\left(\frac{(\gamma-i\omega_{ad})}{\sqrt{2}\delta\omega}\right)}{\delta\omega(\gamma - i\omega_{ad})} \right| \quad (2)$$

describes the anti-diagonal spectral lineshape, while the diagonal one reads as

$$S_D(\omega_d) = \sum_j \alpha_j \left| \frac{\exp\left(\frac{(\gamma - i(\omega_d - \omega_j))^2}{2\delta\omega^2}\right)}{\gamma\delta\omega} \right. \\ \left. \times \left[\operatorname{erfc}\left(\frac{(\gamma - i(\omega_d - \omega_j))}{\sqrt{2}\delta\omega}\right) + \exp\left(\frac{2\gamma i(\omega_d - \omega_j)}{\delta\omega^2}\right) \operatorname{erfc}\left(\frac{(\gamma + i(\omega_d - \omega_j))}{\sqrt{2}\delta\omega}\right) \right] \right|. \quad (3)$$

Here erfc corresponds to the complementary error function, ω_{ad} and ω_d are the anti-diagonal and diagonal angular frequencies, respectively, and $\delta\omega$ characterizes the inhomogeneous distribution. The sum in equation 3 runs over the relative amplitudes α_j and the central diagonal energies ω_j of optical transitions of excitons A, A', B and B*. In equation 2, ω_{ad} is the anti-diagonal frequency offset from the diagonal.

The spectrum of the pulses used for this experiment is displayed on top of the linear absorption spectrum in Fig. 1b. The excitation spectrum exclusively covers the excitonic absorption features, thus guaranteeing the absence of contributions from photocarriers. The 2D map of the absolute value of the rephasing signal from $(\text{PEA})_2\text{PbI}_4$ at 5 K and a fluence of 40 nJ/cm^2 (excitation density $8.8 \times 10^{18} \text{ cm}^{-3}$ or $3.5 \times 10^{13} \text{ cm}^{-2}$) is shown in Fig. 1c. The corresponding real components for different fluences are shown in Fig. S2 of supplemental information. Details regarding the excitation density calculation are also presented in supplemental information. Four features are observed elongated along the diagonal axis, corresponding to excitons A, A', B and B*. Faint cross-peaks between all excitonic features are also observed indicating that all the transitions share a common ground state. Intriguingly, an intense cross peak at an emission energy of 2.305 eV is also observed for exciton A despite the absence of a feature of comparable strength on the diagonal or in the absorption spectrum. Given the opposite phase of this feature (data shown in Supplemental Information Fig. S2) when compared to the corresponding diagonal peak, it could be attributed to an excited state absorption from a singly bound A exciton to a bound AA biexciton with a binding energy of 37 meV. Previous measurements of biexcitonic binding energies were either restricted to higher lying excitons or spectrally unresolved^{6,9,10} and yielded higher values than the one obtained here. This would imply the existence of a complex biexcitonic spectrum with species-dependent binding energies. We do not address further this biexciton spectral structure in this manuscript.

The diagonal and anti-diagonal cuts at the energies of excitons A, A' and B, along with the best fits to equations 3 and 2, are plotted in Fig. 2a, b and c respectively. The only

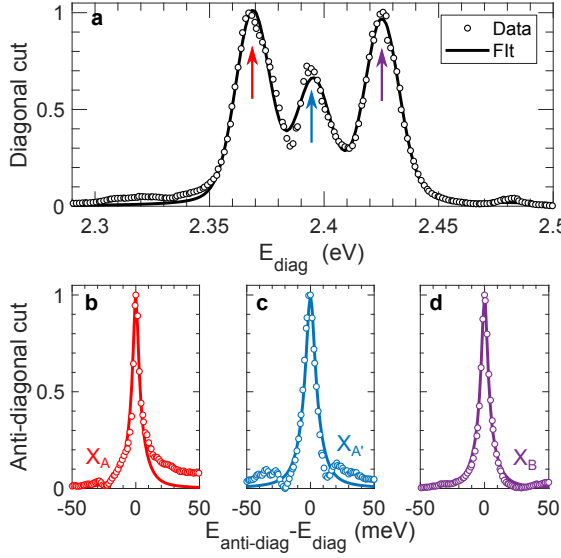


FIG. 2. Fitting diagonal and anti-diagonal cuts to a lineshape model Normalized diagonal cut(a) and anti-diagonal cuts at diagonal energies of excitons A, A' and B (b,c and d respectively) of the two-dimensional coherent excitation rephasing spectrum presented in Fig. 1 c) (circles) and the result of the fitting procedure described in the main text (lines). Arrows in (a) mark the position along the diagonal where the antidiagonal cuts cross it. Due to the presence of low-amplitude cross peaks in the 2D spectrum, these also appear in the tails of the anti-diagonal cuts. To minimize their effect on the quality of the fits and to avoid overestimation of the linewidths, only points higher than 15% of an anti-diagonal cut maxima were included in the fit. The quality of the fits presented here are representative of all the presented dataset. To test the robustness of the fits and to estimate the uncertainties on the extracted linewidths, we repeated the fitting procedure numerous times while adding white noise (5% of the cut's maximum peak to peak) to the data.

fit parameters are the amplitudes α_j , homogeneous dephasing width γ and inhomogeneous width $\delta\omega$ of each optical transition.

To assess the contribution of many-body interactions on the dephasing of the different excitons, we acquired 2D coherent excitation spectra for a wide range of excitation fluences and sample temperatures (see Fig. S3 and S4 of supplemental information for the raw data used here). The dephasing rates of excitons A, A' and B are then estimated via spectral lineshape analysis as detailed above. The monotonic rise of γ with the excitation fluence at 5 K is shown in Fig. 3. Such a dependence is a consequence of broadening induced by

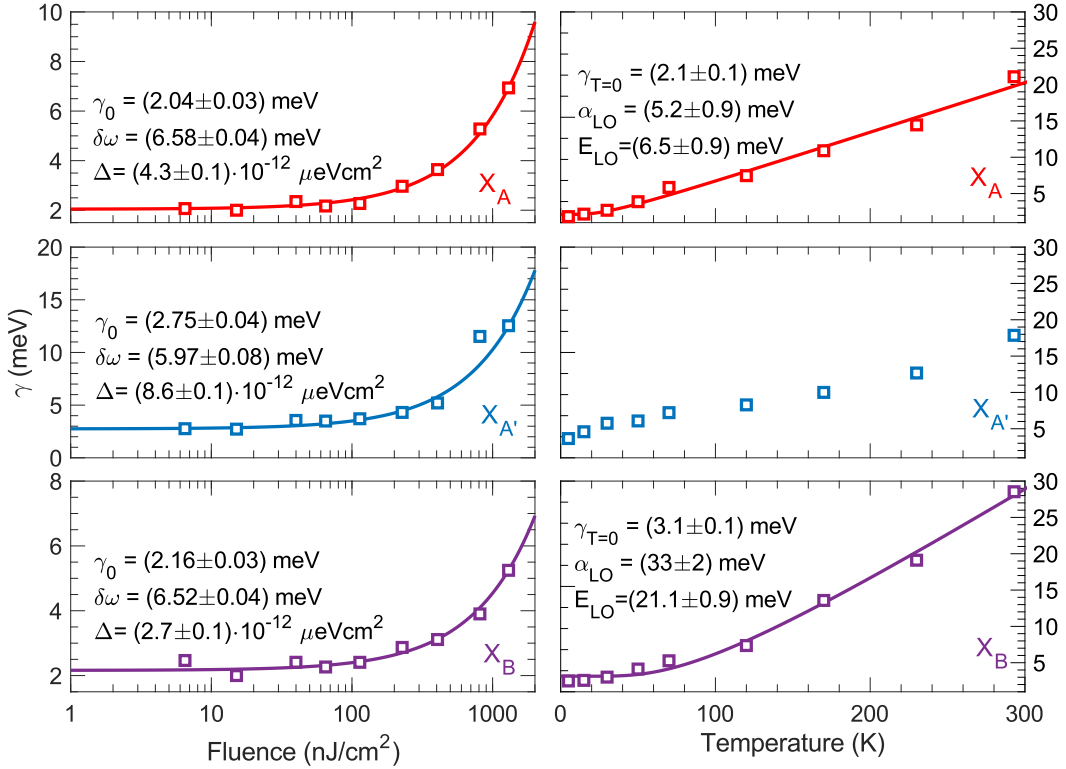


FIG. 3. Fluence and temperature dependence of the exciton dephasing rates. Dephasing parameters γ of excitons A, A' and B (a and d, b and e and c and f respectively) obtained from the simultaneous fitting of diagonal and anti-diagonal cuts, plotted as a function of excitation fluence (a, b and c) or temperature (d, e and f). Squares represent the experimental linewidths and lines are the best fit to the relevant model described in the main text. Error bars on the data are contained within the markers. For a, b and c, the sample's temperature is maintained at 5 K while the excitation fluence is kept at 50 nJ/cm^2 for measurements presented in panels d, e and f.

exciton-exciton elastic scattering, mediated by long-range Coulomb interactions, with the dependence on exciton density n given by

$$\gamma_{\text{EID}}(n) = \gamma_0 + \Delta \cdot n. \quad (4)$$

Here, γ_0 is the density-independent (intrinsic) dephasing rate and Δ is the exciton-exciton interaction parameter. Excitons in 2D metal-halide perovskites are confined to one of the inorganic quantum wells and electronically isolated from the others due to the large distance² ($\sim 8 \text{ \AA}$) imposed between them by the long organic cation. However, the sample itself, 40-nm thick, is composed of tens of these quantum wells, leading to a highly anisotropic

Polarization	γ_A (meV)	$\gamma_{A'}$ (meV)	γ_B (meV)
Horizontal	2.37 ± 0.07	3.89 ± 0.06	2.89 ± 0.07
Left circular	2.70 ± 0.10	4.35 ± 0.08	3.27 ± 0.07
Right circular	2.60 ± 0.10	4.69 ± 0.09	3.40 ± 0.07

TABLE I. Extracted γ for excitons A, A' and B, using linearly or circularly polarized pulses at an excitation fluence of 50 nJ/cm^2 and at 5 K .

exciton-exciton interaction. To allow for some form of comparison with other 2D semiconductors and quasi-two-dimensional quantum wells of similar thicknesses, we report the exciton-exciton interaction parameter, Δ in units of energy per area. The associated fits and the fit parameters are displayed in Fig. 3a, b and c. While γ_0 is approximately 2 meV with a little variance across the three excitonic transitions, Δ varies more substantially. It is around $2.7 \times 10^{-12} \mu\text{eV cm}^2$ for exciton B, increases to $4.3 \times 10^{-12} \mu\text{eV cm}^2$ for exciton A and to $8.6 \times 10^{-12} \mu\text{eV cm}^2$ for exciton A'. It is not straight-forward to compare these values with that of other materials due to the ambiguities over the relevant values of dielectric permittivity function and thus the Bohr radii. However, given the two-dimensional nature of the exciton and comparable exciton binding energies, monolayers of transition metal-dichalcogenides (TMDCs) provide a realistic benchmark. Intriguingly, previous 2D coherent excitation measurements on unencapsulated WSe_2 ³ and encapsulated MoSe_2 ¹¹ revealed $\Delta = 2.7 \times 10^{-12} \text{ meV cm}^2$ and $4 \times 10^{-13} \text{ meV cm}^2$, respectively, three and two orders of magnitude higher than the value obtained here for 2D perovskites. This and the linearity of the dephasing rates over a wide range of excitation densities¹² highlights the substantial screening of the exciton-exciton interactions in these materials. This is especially surprising given the material's relatively high biexciton binding energy,⁶ another characteristic single-layered $(\text{PEA})_2\text{PbI}_4$ shares with TMDCs.^{13,14}

To further highlight the different density-dependent elastic scattering rates for different excitons, we explore the dependence of the laser polarization state on multi-exciton scattering rates. The γ extracted for excitons A, A' and B in these experimental conditions are shown in Table I. For all excitons, γ is consistently smaller with linearly polarized excitation than with circularly polarized pulses. Moreover, except for exciton A', it is independent on the helicity of the exciting pulses within our experimental uncertainty. When exciting the sample

with linearly polarized pulses, excitons can scatter on both left and right circularly polarized excitons. However, they can only scatter with excitons of the same circular polarization when excited with circularly polarized pulses. This demonstrates that angular momentum plays a key role in the Coulomb many-body collisional broadening dynamics,¹² and emphasizes the spectral dependence of these.

We now turn to the temperature dependence of γ to investigate exciton-phonon interactions. The extracted homogeneous linewidths of excitons A, A' and B as a function of sample temperature are presented in Fig. 3d, e and f, respectively. We fit this data with

$$\gamma_{\text{ph}}(T) = \gamma_{T_0} + \alpha_{\text{LO}} \left[\frac{1}{\exp(E_{\text{LO}}/k_B T) - 1} \right], \quad (5)$$

a similar model as that of equation 4. It assumes that line broadening arises from scattering of excitons with a single thermally populated phonon mode of effective energy E_{LO} with an effective interaction parameter α_{LO} . The parameters representing the best fit for each exciton are shown in Fig. 3d and f. This model approximates well the behavior of excitons A and B but fails to reproduce that of exciton A', an indication of the presence of complex lattice interactions as elucidated in some our recent works.^{1,2,6} To compare the strength of the obtained interaction parameters with those of other semiconductors, we obtain the linear interaction parameter Δ_{ph} by taking the low-temperature limit of equation 5, yielding $\Delta_{\text{ph}} = \alpha_{\text{ph}} k_B / E_{\text{LO}}$. This gives linear interaction parameters of 70 ± 20 and $130 \pm 10 \mu\text{eV/K}$ for exciton A and B, respectively. These are almost an order of magnitude larger than in two-dimensional quantum wells^{15,16} and curiously comparable to monolayers of (covalent) TMDCs³ in spite of the ionic character of the lattice and the resultant strong electron-phonon coupling.

Despite the strong polaronic dressing of the excitons with distinct yet multiple phonon modes,² here we find that only one phonon effective energy dominates the scattering process and importantly via weak interactions. Exciton A, dressed primarily by the in-plane lattice modes,² interacts with optical phonons at 6.5 meV, which correspond to lattice modes within the inorganic lead-halide network. Exciton B, which is predominantly dressed by out-of-plane lattice modes,² interacts with higher-energy phonons at 21 meV, which we have identified to have large contributions from the motion of the organic cation, particularly from the $\pi-\pi$ motion of the phenyl groups.¹⁷ This behavior only highlights the complex phonon coupling scenario which may be beyond a conventional Fröhlich formalism and calls

for further experimental and theoretical investigations.

We consider polaronic effects to rationalize the two peculiar observations of this work in the context of many-body interactions in 2D perovskites. Remarkably low inter-exciton scattering rates along with relatively weak exciton-phonon interactions may be attributed to a polaronic protection mechanism,^{18,19} where Coulomb interactions that are at the heart of both these scattering events are effectively screened by the dynamic lattice motion. Such a mechanism has been invoked in the case of bulk 3D perovskites to explain slow cooling of hot carriers²⁰ and long carrier lifetimes,^{21,22} and analogous comparisons can be drawn in their 2D counterparts. Presence of an exciton reorganizes the lattice along well-defined configurational coordinates, which dresses the exciton with a phonon-cloud. Although we currently do not have a reliable estimate of the spatial extent of the deformation, i.e., the polaron radius, based on the polaron coupling constants in lead-halide perovskites, we may hypothesize that the radius is much larger than the exciton size. Such polaronic contributions effectively screen the exciton-exciton interactions. At relatively large densities that are not investigated in the current work, we will have the probability of having two excitons within the polaron radius, in which case biexcitons may be populated given the large biexciton binding energy.⁶ Such density may be substantial and challenging to achieve to realistically implement low-threshold biexciton lasers.²³

Lastly, we note that the zero-density (γ_0) and the zero-temperature ($\gamma_{T=0}$) dephasing widths for all the excitonic transitions are between 2–3 meV, which corresponds to a dephasing time $T_2^* = \hbar/\gamma_{0,T=0} \approx 500$ fs. Time-resolved photoluminescence measurements performed at 5 K have revealed a lower limit for the exciton lifetime to be around 100 ps,²⁴ suggesting a radiative width $\gamma_{\text{rad}} \sim 0.04$ meV, which is much lower than the measured lower-limit $\gamma_{0,T=0}$. This clearly demonstrates the presence of an additional dephasing mechanism in addition to inter-exciton and phonon scattering, possibly due to the defective nature of the polycrystalline film, the presence of other degenerate dark states which excitons scatter in and out of, or via low-energy acoustic phonons unresolved in the current experiment. Long exciton coherences close to the radiative limit are being constantly pursued in the context of material applications in quantum information and photonics. The relatively short dephasing rates observed here may set a fundamental barrier for realistic implementation of these material systems in quantum opto-electronics, including as single photon emitters.²⁵

In a general sense, many-body exciton interactions are determined by an interplay of

Coulomb forces. We have focused on the comparison of elastic scattering processes in distinct excitons within the spectral fine structure, manifested via the dephasing rate. In a previous publication, we have reported high biexciton binding energies in this material,⁶ and importantly, that biexcitons display distinct spectral structure. We highlight that in ref. 6, the biexciton binding energy of excitons A and B appears to be different, and exciton A displays clear evidence of repulsive interactions in the two-quantum, two-dimensional spectral correlation map. Such interactions might give rise to inelastic scattering of exciton A, perhaps related to Auger recombination.⁴ These overlapping dynamics would be deterministic in biexciton lasers,²³ for example, if these devices were to be rigorously implemented. The extent to which the spectral scattering rates depend on spectral structure might also determine the dynamics of exciton polaritons in semiconductor microcavities, in which polariton condensates are formed by polariton-polariton inelastic scattering.²⁶ It has been demonstrated that polariton-polariton interactions in 2D lead-halide perovskites are strong,²⁷ and distinct in-plane and out-of-plane polaritons have been identified.²⁸ We consider that it would be fundamentally important in the advent of room-temperature polariton condensation to determine how the lattice-driven identity of multiple excitons and their distinct quantum dynamics translate into polariton-polariton quantum dynamics driving room-temperature condensates.

¹ Neutzner, S. *et al.* Exciton-polaron spectral structures in two-dimensional hybrid lead-halide perovskites. *Physical Review Materials* **2**, 064605 (2018).

² Thouin, F. *et al.* Phonon coherences reveal the polaronic character of excitons in two-dimensional lead halide perovskites. *Nature Materials* **11**, 349–356 (2019).

³ Moody, G. *et al.* Intrinsic homogeneous linewidth and broadening mechanisms of excitons in monolayer transition metal dichalcogenides. *Nature Communications* **6**, 8315 (2015).

⁴ Xing, G. *et al.* Transcending the slow bimolecular recombination in lead-halide perovskites for electroluminescence. *Nature Communications* **8**, 14558 (2017).

⁵ Turner, D. B. & Nelson, K. A. Coherent measurements of high-order electronic correlations in quantum wells. *Nature* **466**, 1089 (2010).

⁶ Thouin, F. *et al.* Stable biexcitons in two-dimensional metal-halide perovskites with strong

dynamic lattice disorder. *Physical Review Materials* **2**, 034001 (2018).

⁷ Siemens, M. E., Moody, G., Li, H., Bristow, A. D. & Cundiff, S. T. Resonance lineshapes in two-dimensional Fourier transform spectroscopy. *Optics Express* **18**, 17699–17708 (2010).

⁸ Bristow, A. D., Zhang, T., Siemens, M. E., Cundiff, S. T. & Mirin, R. P. Separating homogeneous and inhomogeneous line widths of heavy- and light-hole excitons in weakly disordered semiconductor quantum wells. *The Journal of Physical Chemistry B* **115**, 5365–5371 (2011).

⁹ Elkins, M. H. *et al.* Biexciton resonances reveal exciton localization in stacked perovskite quantum wells. *Journal of Physical Chemistry Letters* **8**, 3895–3901 (2017).

¹⁰ Ishihara, T., Hong, X. & Ding, J. Dielectric confinement effect for exciton and biexciton states in Pbla-based two-dimensional semiconductor structures. *Surface Science* **267**, 323–326 (1992).

¹¹ Martin, E. W. *et al.* Encapsulation narrows excitonic homogeneous linewidth of exfoliated MoSe₂ monolayer (2018). ArXiv:1810.09834 [cond-mat.mtrl-sci].

¹² Ciuti, C., Savona, V., Piermarocchi, C., Quattropani, A. & Schwendimann, P. Role of the exchange of carriers in elastic exciton-exciton scattering in quantum wells. *Physical Review B* **58**, 7926–7933 (1998).

¹³ You, Y. *et al.* Observation of biexcitons in monolayer WSe₂. *Nature Physics* **11**, 477–482 (2015).

¹⁴ Kylnp, I. & Komsa, H.-P. Binding energies of exciton complexes in transition metal dichalcogenide monolayers and effect of dielectric environment. *Physical Review B* **92**, 205418 (2015).

¹⁵ Honold, A., Schultheis, L., Kuhl, J. & Tu, C. W. Collision broadening of two-dimensional excitons in a GaAs single quantum well. *Physical Review B* **40**, 6442–6445 (1989).

¹⁶ Wagner, H. P., Schtz, A., Maier, R., Langbein, W. & Hvam, J. M. Coherent optical nonlinearities and phase relaxation of quasi-three-dimensional and quasi-two-dimensional excitons in ZnS_xSe_{1-x}/ZnSe structures. *Physical Review B* **56**, 12581–12588 (1997).

¹⁷ Alexandru Dragomir, V. *et al.* Lattice vibrations and dynamic disorder in two-dimensional hybrid lead-halide perovskites (2018). ArXiv:1812.05255 [cond-mat.mtrl-sci].

¹⁸ Zhu, X.-Y. & Podzorov, V. Charge carriers in hybrid organicinorganic lead halide perovskites might be protected as large polarons. *The Journal of Physical Chemistry Letters* **6**, 4758–4761 (2015).

¹⁹ Miyata, K. *et al.* Large polarons in lead halide perovskites. *Science Advances* **3**, e1701217 (2017).

²⁰ Joshi, P. P., Maehrlein, S. F. & Zhu, X. Dynamic screening and slow cooling of hot carriers in lead halide perovskites. *Advanced Materials* **1803054** (2019).

²¹ Wehrenfennig, C., Liu, M., Snaith, H. J., Johnston, M. B. & Herz, L. M. Charge-carrier dynamics in vapour-deposited films of the organolead halide perovskite $\text{CH}_3\text{NH}_3\text{PbI}_{3-x}\text{Cl}_x$. *Energy Environ. Sci.* **7**, 2269–2275 (2014).

²² Brenner, T. M. *et al.* Are mobilities in hybrid organic–inorganic halide perovskites actually “high”? *The Journal of Physical Chemistry Letters* **6**, 4754–4757 (2015).

²³ Booker, E. P. *et al.* Vertical cavity biexciton lasing in 2D dodecylammonium lead iodide perovskites. *Advanced Optical Materials* **6**, 1800616 (2018).

²⁴ Straus, D. B. *et al.* Direct observation of electron-phonon coupling and slow vibrational relaxation in organic–inorganic hybrid perovskites. *Journal of the American Chemical Society* **138**, 13798–13801 (2016).

²⁵ Utzat, H. *et al.* Coherent single-photon emission from colloidal lead halide perovskite quantum dots. *Science* **363**, 1068–1072 (2019).

²⁶ Carusotto, I. & Ciuti, C. Quantum fluids of light. *Reviews of Modern Physics* **85**, 299–368 (2013).

²⁷ Fieramosca, A. *et al.* Two-dimensional hybrid perovskites sustaining strong polariton interactions at room temperature (2018). ArXiv:1811.04041 [physics.optics].

²⁸ Fieramosca, A. *et al.* Tunable out-of-plane excitons in 2D single-crystal perovskites. *ACS Photonics* **5**, 4179–4185 (2018).

²⁹ Turner, D. B., Stone, K. W., Gundogdu, K. & Nelson, K. A. Invited Article: The coherent optical laser beam recombination technique (COLBERT) spectrometer: Coherent multidimensional spectroscopy made easier. *Review of Scientific Instruments* **82**, 081301 (2011).

³⁰ Loriot, V., Gitzinger, G. & Forget, N. Self-referenced characterization of femtosecond laser pulses by chirp scan. *Optics Express* **21**, 24879–24893 (2013).

ACKNOWLEDGMENTS

A.R.S.K. acknowledges funding from EU Horizon 2020 via a Marie Skłodowska Curie Fellowship (Global) (Project No. 705874). This work is partially supported by the National Science Foundation (Award 1838276). C.S. acknowledges support from the School of Chemistry and Biochemistry and the College of Science of Georgia Institute of Technology.

AUTHOR CONTRIBUTIONS

F.T. carried out all measurements and performed the analysis of the experimental data. D.C. synthesized the samples. A.P. supervised the sample preparation activity. C.S. and A.R.S.K. supervised the ultrafast spectroscopy activity. A.R.S.K. and C.S. conceived the project. All authors contributed to the redaction of the manuscript. C.S. and A.R.S.K. are to be considered corresponding co-authors.

METHODS

Sample preparation

Thin films of $(\text{PEA})_2\text{PbI}_4$ (thickness of 40 nm) were prepared on sapphire substrates (optical windows 25 mm \times 0.5 mm, Crystran) by spin coating a 0.05 M solution of the perovskite in N,N-Dimethylformamide (DMF). 12.5 mg of (PEA)I (Dyesol) was mixed with 11.5 mg PbI_2 (TCI) and dissolved in 500 μl of DMF (Sigma Aldrich, anhydrous, 99.8%). The solution was left to dissolve on a hotplate at 100°C for 1 hour. After exposing the substrate under oxygen plasma, the solution (kept at 100°C) was spin coated on the sapphire window at 6000 rpm, 30 s, and the film was annealed on a hotplate at 100°C for 15 minutes. Solution and film preparation were performed in a glove-box under N_2 inert atmosphere.

Multidimensional spectroscopy

The pulses used for these measurements were generated by a home-built single pass non-collinear optical parametric amplifier powered by a ultrafast laser system (Pharos Model PH1-20-0200-02-10, Light Conversion) emitting 1,030-nm pulses at 100 kHz, with an output

power of 20 W and pulse duration of 220 fs. Multidimensional spectroscopic measurements were carried on using a home-built implementation of COLBERT,²⁹ a pulse-shaper-based multidimensional spectrometer that passively stabilizes the relative phase of each pulses. Each beams was independently compressed using chirp-scan³⁰ to a pulse duration of 20 fs FWHM, measured using cross-correlated second harmonic frequency resolved optical gating (SH-XFROG) in a 10 μ m-thick BBO crystal placed at the sample position. A typical SH-XFROG trace is shown in Fig. S5 of Supplemental Information. The sample was kept at cryogenic temperatures using a vibration-free cold-finger closed-cycle cryostat from Montana Instruments.

**Supplemental information for Spectral structure in the
many-body elastic Coulomb scattering rates of excitons in
two-dimensional metal-halide hybrid perovskites**

Félix Thouin,¹ Daniele Cortecchia,² Annamaria Petrozzi,²

Ajay Ram Srimath Kandada,² and Carlos Silva^{3,1}

¹*School of Physics, Georgia Institute of Technology,
837 State Street NW, Atlanta, Georgia 30332, United States*

²*Center for Nano Science and Technology@Polimi,
Istituto Italiano di Tecnologia, via Giovanni Pascoli 70/3, 20133 Milano, Italy*

³*School of Chemistry and Biochemistry,
Georgia Institute of Technology, 901 Atlantic Drive NW,
Atlanta, Georgia 30332, United States*

(Dated: April 28, 2019)

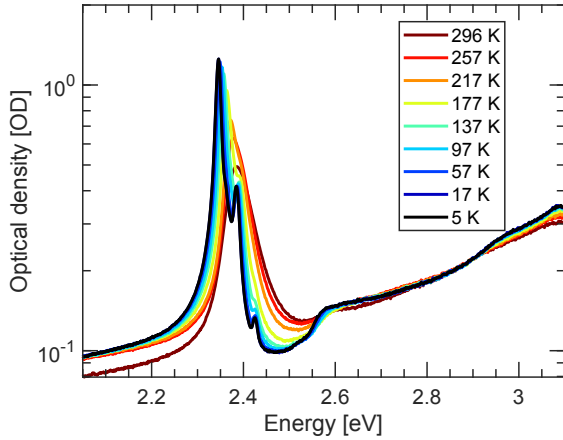


FIG. S1. Temperature dependent absorption spectra on a logarithmic scale.

ESTIMATION OF THE INDUCED EXCITATION DENSITY

The presence of spectral features in the absorption spectra as well as the pulses' non-uniform spectra must be accounted for when calculating the excitation density induced by one pulse. We do so by calculating the fluence to surface excitation density factor Θ as

$$\Theta = \int_0^{\infty} \frac{A(E)P(E)}{E} dE \quad (1)$$

where $A(E)$ is the absorption spectrum, $P(E)$ is the pulse spectrum normalized so that its integral yields unity and E the energy. To obtain the surfacic excitation density, we then multiply the pulse fluence by Θ . The volumic excitation density is then obtained by dividing this number by the thickness of the material, namely 40 nm. We obtained a value of 8.75×10^{20} excitons per J for Θ .

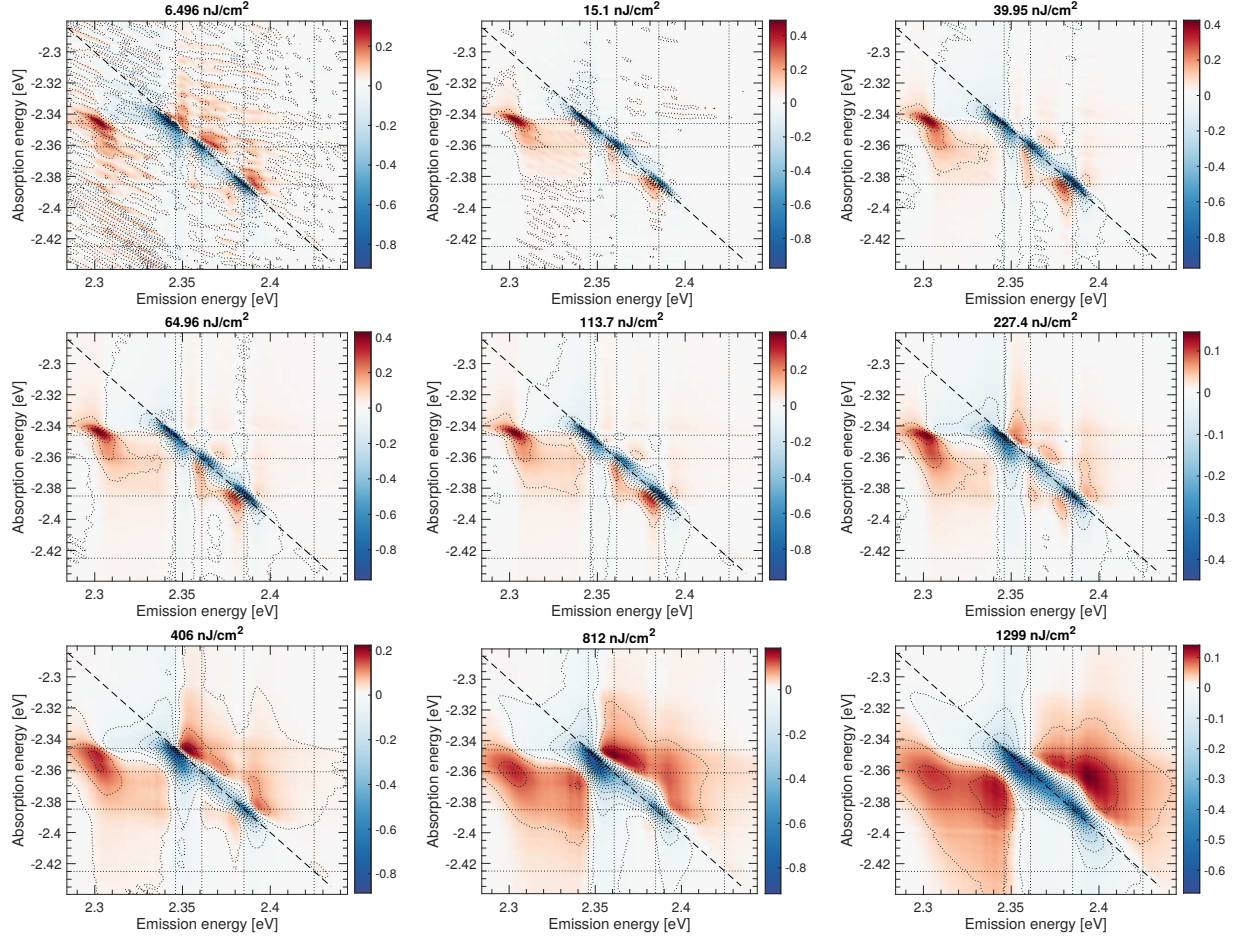


FIG. S2. Real part of fluence dependent photon-echo spectra at 5 K. The signal was phased at an emission energy of 2.385 eV. Each spectrum was normalized by the maximal value of its norm.

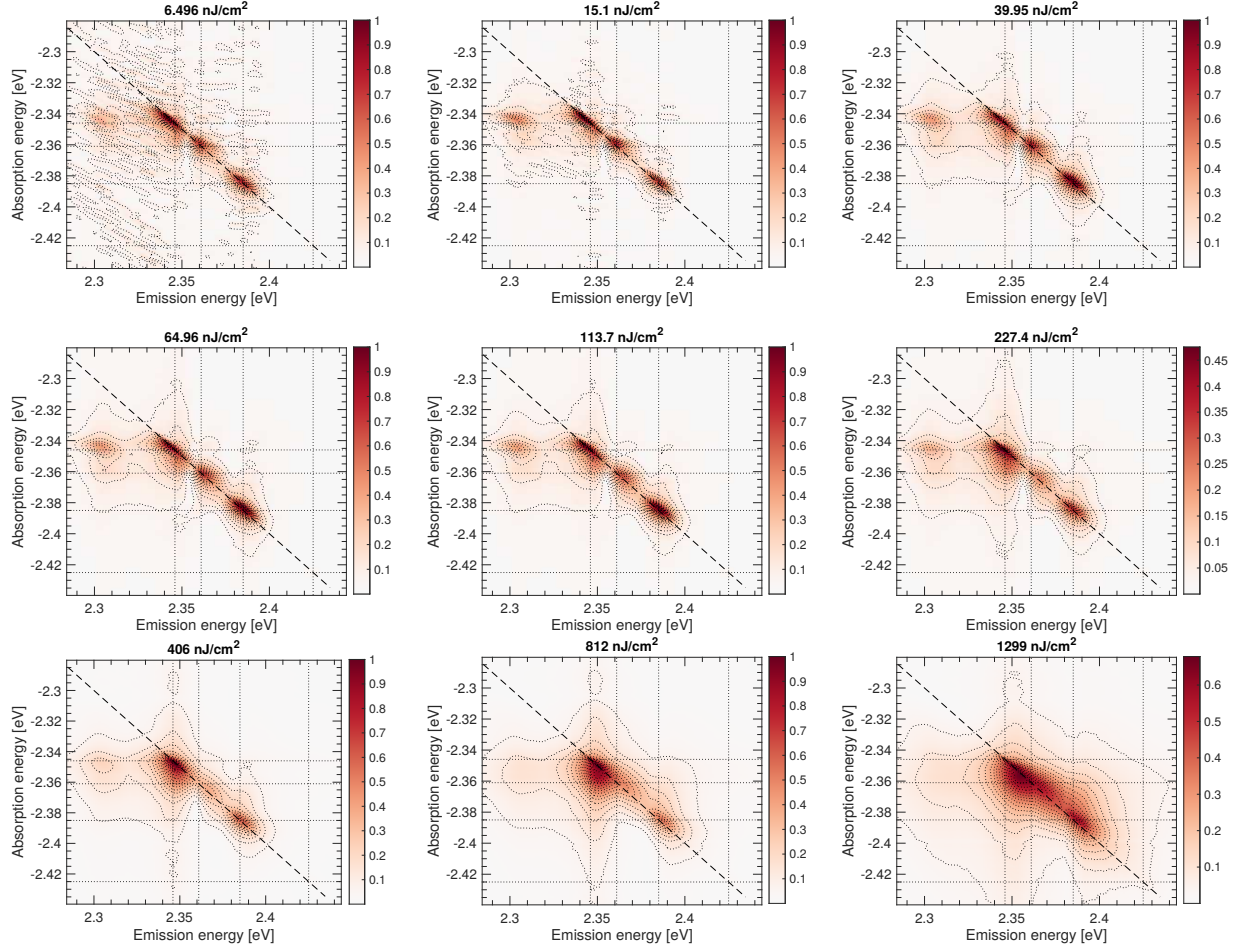


FIG. S3. Norm of fluence dependent photon-echo spectra at 5 K. Each spectrum was normalized by the maximal value of its norm.

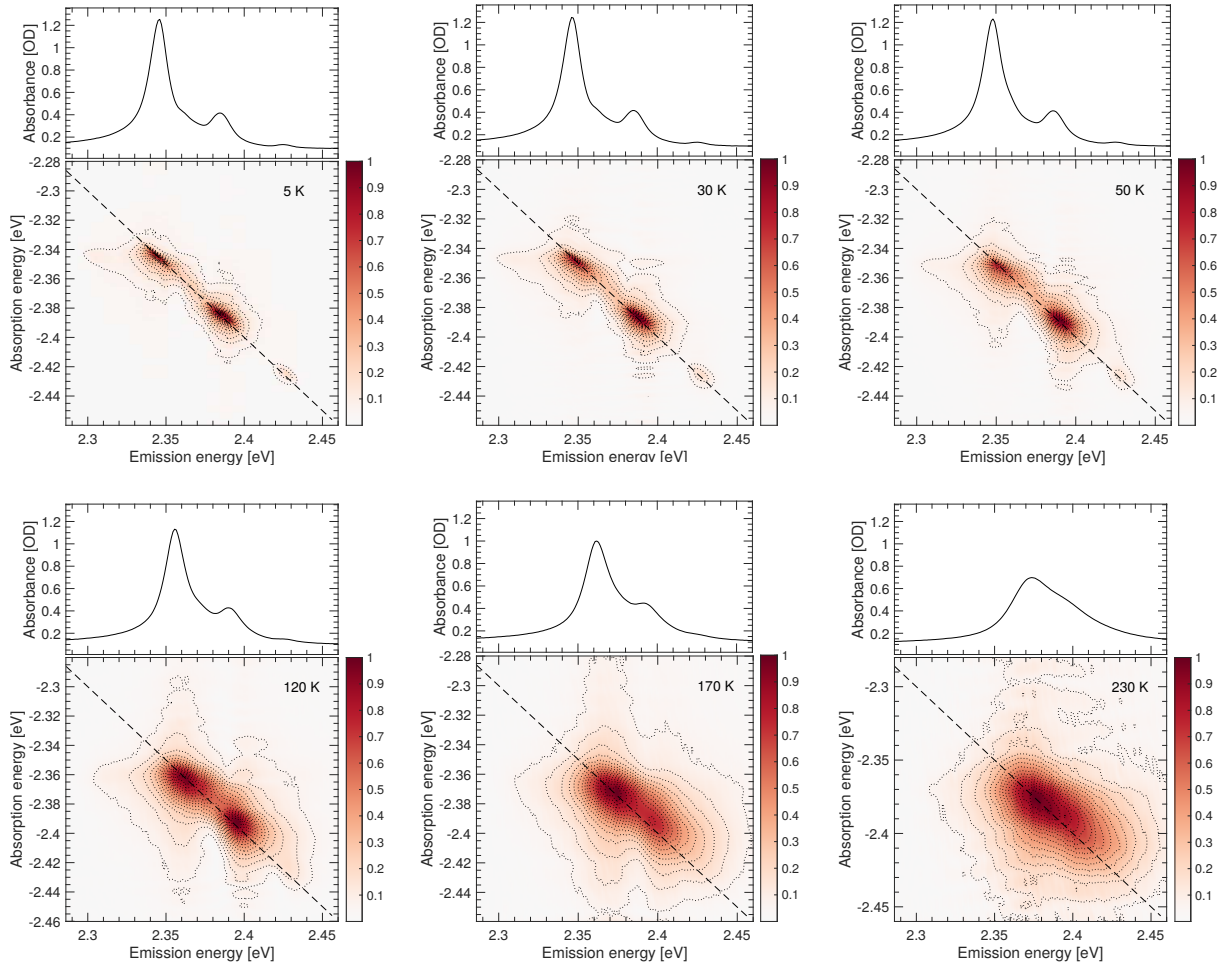


FIG. S4. Norm of temperature dependent photon-echo spectra at 5 K. Each spectrum was normalized by the maximal value of its norm. The corresponding absorption spectrum is plotted above each photon-echo spectra.

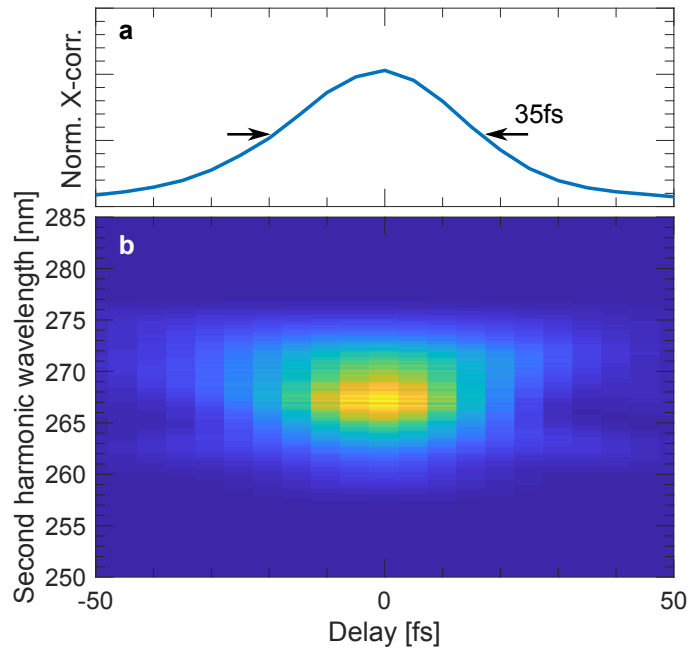


FIG. S5. (a) Cross-correlation of one the pulses used in the experiments with the local oscillator pulse. it is obtained by spectrally integrating the SH-XFROG measurement. The FWHM of the cross-correlation is 35 fs, yielding a pulse duration of 25 fs. (b) SH-XFROG trace of one of the pulses with the LO pulse.